Measurements of the Ground-State Polarizabilities of Cs, Rb, and K using Atom Interferometry

Maxwell D. Gregoire,[1] Ivan Hromada,[1] William F. Holmgren,[1] Raisa Trubko,[2] and Alexander D. Cronin[1,2]

[1] *Department of Physics, University of Arizona, Tucson, AZ 85721*
[2] *College of Optical Sciences, University of Arizona, Tucson, AZ 85721*

(Dated: September 3, 2015)

We measured the ground-state static electric-dipole polarizabilities of Cs, Rb, and K atoms using a three-nanograting Mach-Zehnder atom beam interferometer. Our measurements provide benchmark tests for atomic structure calculations and thus test the underlying theory used to interpret atomic parity non-conservation experiments. We measured $\alpha_{\rm Cs} = 4\pi\epsilon_0 \times 59.45(11)\text{Å}^3$, $\alpha_{\rm Rb} = 4\pi\epsilon_0 \times 47.44(9)\text{Å}^3$, and $\alpha_{\rm K} = 4\pi\epsilon_0 \times 42.97(8)\text{Å}^3$. We report ratios of polarizabilities $\alpha_{\rm Cs}/\alpha_{\rm Rb} = 1.2532(10)$, $\alpha_{\rm Cs}/\alpha_{\rm K} = 1.3835(9)$, and $\alpha_{\rm Rb}/\alpha_{\rm K} = 1.1040(9)$ with smaller fractional uncertainty because the systematic errors for individual measurements are largely correlated. Since Cs atom beams have short de Broglie wavelengths, we developed measurement methods that do not require resolved atom diffraction. Specifically, we used phase choppers to measure atomic beam velocity distributions, and we used electric field gradients to give the atom interference pattern a phase shift that depends on atomic polarizability.

I. INTRODUCTION

High-precision measurements of static electric-dipole polarizabilities serve as benchmark tests for *ab initio* calculations of electric-dipole transition matrix elements. These calculations require understanding quantum many-body systems with relativistic corrections, and there are many different methods that attempt to calculate these matrix elements in a reasonable amount of computing time [1]. Testing these methods is important because these matrix elements are used to calculate many atomic properties, such as lifetimes, oscillator strengths, line strengths, van der Waals interaction potentials and associated cross sections, Feshbach resonances, and photoassociation rates. Measuring alkali static polarizabilities as a means of testing atomic structure calculations has been of interest to the physics community since Stark's pioneering measurements in 1934 [2]. Static polarizabilities have been measured using deflection [2–5], E-H gradient balance [6, 7], time-of-flight of an atomic fountain [8], and phase shifts in atomic and molecular interferometers [9–12].

We measured the static electric-dipole polarizabilities of K, Rb, and Cs atoms with 0.19% uncertainty using a Mach-Zehnder three-grating atom interferometer [13, 14] with an electric field gradient interaction region. We used the same apparatus for all three atomic species, so we can also report polarizability ratios with 0.08% uncertainty because the sources of systematic uncertainty are largely correlated between our measurements of different atoms' polarizabilities.

We compare our measurements to polarizability values of similar uncertainty deduced from studies of atomic lifetimes, Feshbach resonances, and photoassociation specroscopy. Then we analyze our measurements to report the Cs $6p_{1/2}$ and $6p_{3/2}$ state lifetimes, Rb $5p_{1/2}$ and $5p_{3/2}$ state lifetimes, and K $4p_{1/2}$ and $4p_{3/2}$ state lifetimes, as well as the associated principal electric dipole matrix elements, oscillator strengths, and line strengths. We also use our measurements to report van der Waals C_6 coefficients, and we combine our measurements with recent measurements of transition Stark shifts to report some excited state polarizabilities with better than 0.1% uncertainty.

Testing Cs atomic structure calculations by measuring $\alpha_{\rm Cs}$ is valuable for atomic parity non-conservation (PNC) research, which places constraints on beyond-the-standard-model physics. The coupling strength, $E_{\rm PNC}$, of Z^0-mediated interactions between the Cs valence electron and the neutrons in its nucleus can be written in terms of the electric dipole transition matrix elements and the nuclear weak charge parameter Q_W. Atomic structure calculations are needed to deduce a value of Q_W from an $E_{\rm PNC}$ measurement [15] to compare to the Q_W predicted by the standard model [16, 17]. Our measurement of $\alpha_{\rm Cs}$ tests the methods used to calculate the relevant matrix elements and provides a benchmark for the $\left\langle 6s_{1/2}\right|\left|\hat{D}\right|\left|6p_{1/2}\right\rangle$ matrix element, one of the terms in the expression for $E_{\rm PNC}$.

This is the first time that atom interferometry measurements of polarizability have been reported with smaller fractional uncertainty than the pioneering $\alpha_{\rm Na}$ measurement by Ekstrom *et al.* in 1995 [9]. This is also, to our knowledge, the first time atom interferometry has been used to measure Cs polarizability. The latter is in part because it is challenging to resolve Cs atomic diffraction; our nanogratings diffract our Cs atom beams with only $4 \cdot 10^{-5}$ rad between diffraction orders. Because of this small diffraction angle, we designed an experiment with an electric field gradient instead of a septum electrode, such as that used in [9]. We developed phase choppers [19–22] to measure our atom beams' velocity distributions instead of measuring velocity distributions

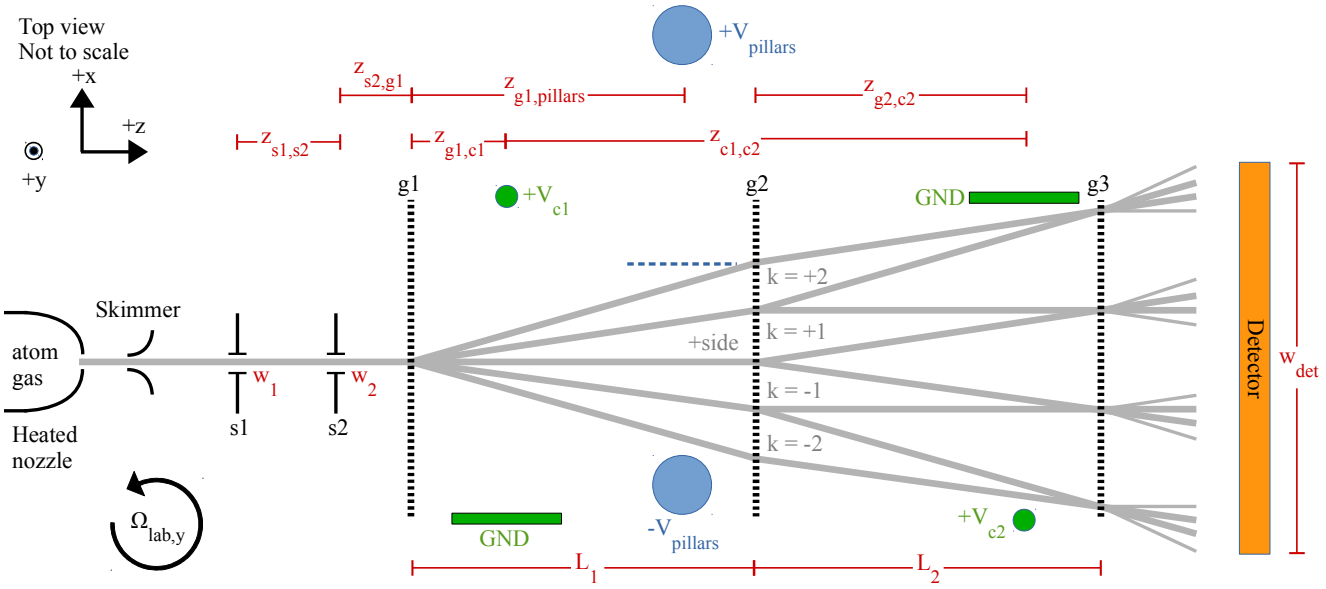

FIG. 1. (Color online) Diagram of the Mach-Zehnder atom interferometry apparatus. Dimensions are shown in red and tabulated in Table I. The supersonic atom beam, shown in gray, is collimated by two slits s1 and s2 with widths w_1 and w_2 before entering the first grating. The nanogratings, g1, g2, and g3, are spaced longitudinally such that $L_1 = L_2$, which causes an interference pattern to form at the position of g3. We consider the four separate interferometers in our data analysis, labeled with $k = +2, +1, -1, -2$, that form via 0th, 1st, and 2nd order diffraction from g1. The atoms are detected by a platinum Langmuir-Taylor detector [18], indicated in orange. The pair of blue circles represents oppositely-charged cylindrical electrodes (extending perpendicular to the page) that form a virtual ground plane between them. The electric field from these electrodes polarizes the atoms and thereby shifts the interference pattern's phase. The phase choppers are shown in green; each phase chopper is a charged wire next to a grounded plane. The geometry terms relevant to the pillars and phase choppers are displayed in Fig. 2 and discussed in section II.a. Due to the rotation of the Earth, the lab has a rotation rate about the vertical axis of $\Omega_{\mathrm{lab},y} = 38.88\ \mu$rad/s.

by studying atom diffraction patterns [9, 11]. These two innovations enable us to measure polarizabilities of heavy atoms such as Cs without resolving diffraction patterns. Without the need to resolve diffraction, we can use larger collimating slits and a wider detector obtain data more quickly. These innovations also reduce some systematic errors related to beam alignment imperfections.

We improved the accuracy of our measurements compared to our previous work [11] by redesigning the electrodes that apply phase shifts to our interferometer. The new configuration of electrodes, two parallel, oppositely-charged cylinders, allows us to determine the distance between the beam and the ground plane with reduced statistical uncertainty. We reduced systematic error by making higher-accuracy measurements of the width of the gap between the pillars, the pillars' radius, the voltages on the pillars, and the distance between the pillars and the first grating. Our more accurate measurements required a more sophisticated model of the apparatus, which included interference formed by ±1st and ±2nd order diffraction, the finite thickness and divergence of the beam, and the finite width of the detector [22]. Our higher-accuracy measurements also required us to develop a more detailed error analysis, which led us to add an additional calibration step to our measurement procedure in which we precisely measure and set the distances between nanogratings in our interferometer.

II. APPARATUS DESCRIPTION AND ERROR ANALYSIS

A schematic diagram of the three-grating Mach-Zehnder atom beam interferometer we use to make our measurements is shown in Fig. 1. A mix of He and Ar gas carries Cs, Rb, or K vapor through a 50 μm nozzle to generate a supersonic atom beam [23][24]. We adjust the carrier gas composition to change the beam's average velocity: a higher percentage of Ar results in a slower beam. The atom beam passes through two collimating slits and diffracts through three silicon nitride nanogratings, each with period $d_g = 100$ nm. The first two gratings manipulate the atoms' de Broglie waves to form a 100 nm-period interference pattern at the position of the third grating. The third grating acts as a mask for that interference pattern. The method of observing interference fringes is described in detail in [25]: we scan the second grating in the $\pm x$ direction and observe the flux admitted through the third grating in order to determine the interference pattern's contrast and phase. We measure that trans-

TABLE I. List of apparatus dimensions described in Fig. 1 and Fig. 2. Dimensions with no quoted uncertainty have uncertainty much less than what would be significant to our analysis. a_{c1} and a_{c2} are the closest distances between the wires and the ground planes for phase choppers 1 and 2, and a_{pillars} is half the width of the gap between the pillars (the closest distance between the virtual ground plane and either pillar). $L_1 - L_2 = 0 \pm 30$ μm, and the uncertainty in $L_1 + L_2$ is insignificant.

$z_{\text{s1,s2}}$	860 mm
$z_{\text{g1,pillars}}$	833.5 ± 0.25 mm
$z_{\text{g1,c1}}$	269.7 mm
$z_{\text{s2,g1}}$	100 mm
$z_{\text{g2,c2}}$	598 mm
$z_{\text{c1,c2}}$	1269.3 ± 0.25 mm
L_1	940 mm
L_2	940 mm
w_1	30 ± 6 μm
w_2	40 ± 6 μm
w_{det}	100 ± 20 μm
a_{pillars}	1999.85 ± 0.5 μm
R_{pillars}	6350 ± 0.5 μm
a_{c1}	986 ± 25 μm
R_{c1}	785.5 μm
a_{c2}	893 ± 25 μm
R_{c2}	785.5 μm

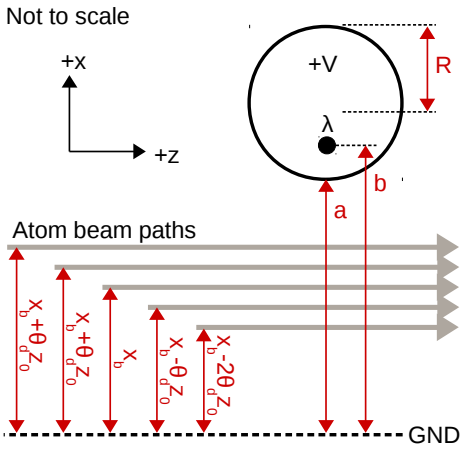

FIG. 2. (Color online) Diagram showing the dimensions, shown in red, that describe the static electric fields created by the pillars and by the phase choppers. The circle represents the cross-section of a metal pillar or charged wire with radius R held at voltage V. The GND line represents the ground plane, which may by physical (in the case of the choppers) or virtual (in the case of the pillars). a is the closest distance between the pillar edge and the ground plane. The parameter b is the distance between the ground plane and the effective line charge within the pillar. The atom beam center is a distance x_b away from the ground plane. The different interferometer arms are separated from their neighbors by multiples of $\theta_d z_0$, where θ_d is the diffraction angle and z_0 is the longitudinal distance to whichever is closer: g1 or g3. a and R dimensions for the pillars and phase choppers are given in Table I.

mitted atomic flux with a 100 μm-wide platinum wire Langmuir-Taylor detector [18].

In the rest of Section II we describe how we measure the atoms' velocity distribution and polarizability. We measure v_0, the atoms' mean velocity, using phase choppers, which are charged wires parallel with the y axis held parallel to grounded planes, indicated in green in Fig. 1. We measure static polarizability α with a non-uniform electric field created by two oppositely charged stainless-steel cylinders, hereby referred to as "pillars", parallel with the y axis and indicated in blue in Fig. 1. The pillars' electric field shifts the phase by an amount roughly proportional to α/v_0^2. Section II.a. describes how the electric field geoemtry of both the phase choppers and the pillars causes a differential phase shift. Section II.b. describes how we use the phase choppers to measure the velocity distribution, and section II.c. describes how we use the pillars to measure α. Section II.d. discusses how we apply our knowledge of the velocity distribution to analysis of the data taken with the pillars.

II.a. Phase shifts with cylindrical electrodes

Both the pillars and the phase choppers are described by the geometry shown in Fig. 2, and create electric fields given by

$$\vec{E}(x,z) = \frac{\lambda}{2\pi\epsilon_0}\left[\frac{x-b}{(x-b)^2+z^2} - \frac{x+b}{(x+b)^2+z^2}\right]\hat{x} + \left[\frac{z}{(x-b)^2+z^2} - \frac{z}{(x+b)^2+z^2}\right]\hat{z} \quad (1)$$

where the effective line charge density

$$\lambda = 2\pi\epsilon_0 V \ln^{-1}\left(\frac{a+R+b}{a+R-b}\right) \quad (2)$$

exists a distance $b = a\sqrt{1+2R/a}$ away from the ground plane. The parameter a represents the distance between the ground plane and the closest cylinder edge, R represents the pillars' radius, and the directions $\hat{x}$ and $\hat{z}$ are shown in Fig. 2.

When atoms enter an electric field, their total energy changes by $U_{\text{Stark}} = -\frac{1}{2}\alpha|\vec{E}|^2$; thus the electric field represents a region of lower potential energy for those atoms. Since $U_{\text{Stark}} \approx -0.1$ μeV and $E_{\text{kinetic}} \approx 1$ eV in our experiment, we can use the WKB approximation along with the Residue Theorem to compute the total phase accumulated by an atom travelling through the field. We can also approximate that atoms travel tangential to the ground plane regardless of the angle at which

they diffracted and their incident angle upon grating g1. Even though this approximation may be incorrect by up to 10^{-3} rad, such a discrepancy would only cause errors in the accumulated phases by factors of 10^{-6}, which is insignificant for our experiment. Therefore, we represent the accumulated phase along one path for a component of an atomic de Broglie wave as

$$\Phi(v,x) = \frac{1}{\hbar v}\int_{-\infty}^{\infty}\frac{1}{2}\alpha|\vec{E}|^2 dz = \frac{\lambda^2\alpha}{\pi\epsilon_0^2\hbar v}\left(\frac{b}{b^2-x_b^2}\right) \quad (3)$$

where x_b is the distance between the atom's path and the ground plane.

The atoms in our beam form many interferometers, but we only need to consider the four interferometers shown in Fig. 1. Other interferometers are insignificant to our analysis because they have some combination of low contrast and low flux. We label the four interferometers that we do consider with the index $k = +2$, $k = +1$, $k = -1$, and $k = -2$. The differential phase shifts for the four interferometers are

$$\begin{aligned}
\Delta\Phi_{\vec{E},+2}(v,x_b) &= \Phi(v,x_b+2\theta_d z_0) - \Phi(v,x_b+\theta_d z_0)\\
\Delta\Phi_{\vec{E},+1}(v,x_b) &= \Phi(v,x_b+\theta_d z_0) - \Phi(v,x_b)\\
\Delta\Phi_{\vec{E},-1}(v,x_b) &= \Phi(v,x_b) - \Phi(v,x_b-\theta_d z_0)\\
\Delta\Phi_{\vec{E},-2}(v,x_b) &= \Phi(v,x_b-\theta_d z_0) - \Phi(v,x_b-2\theta_d z_0) \quad (4)
\end{aligned}$$

In the above equations, $\theta_d z_0$ is the lateral separation between classical paths in the interferometer, where $\theta_d = \lambda_{\mathrm{dB}}/d_g$ is the diffraction angle and z_0 the distance to whichever of the first or third gratings is closer.

II.b. Velocity measurement

The atoms in the beam do not all have the same velocity, so the electric fields do not apply the same phase shifts to each diffracted atom. We observe the average phase and contrast of an ensemble of atoms with velocity distribution $P(v)$. We model $P(v)$ as a Gaussian distribution

$$P(v)dv = \frac{v_r}{v_0\sqrt{2\pi}}e^{-\frac{v_r^2(v-v_0)^2}{2v_0^2}} \quad (5)$$

where v_0 is the mean velocity and $v_r = v_0/\sigma_v$ is a measure of the distribution's sharpness. It is worth noting that the velocity distribution for a supersonic atom beam is better described by a v^3-weighted Gaussian distribution [13]. However, either distribution can be used in our analysis to parametrize the typical high-v_0, high-v_r velocity distributions of our atom beam without changing our polarizability result by more than 0.008%. Since v_0 is the average velocity in a Gaussian but not in a v^3-weighted Gaussian, we use Eqn. (5) to simplify our discussion of the error analysis.

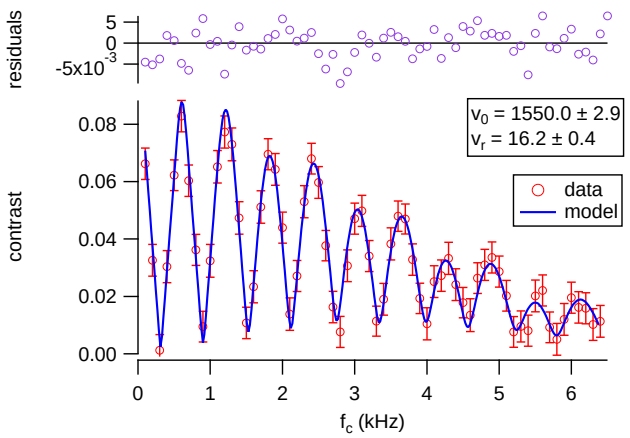

FIG. 3. (Color online) An example of a measurement of contrast C vs. phase chopper frequency f_c for a Cs beam. We fit a model to these data that has v_0 and v_r as fit parameters in order to measure the velocity distribution.

To measure v_0 and v_r, we use phase choppers [21, 22]. Each phase chopper is a charged wire about 1 mm away from a physical ground plane (see Table I for phase chopper dimensions). Chopper c1 is between the first two gratings and chopper c2 is a distance $z_{c1,c2} = 1269.3 \pm 0.25$ mm downstream of chopper c1, between the last two gratings (see Fig. 1). The voltages on the choppers' wires and the distances between the beam and the choppers' ground planes are chosen such that chopper c1 shifts the ensemble's average phase by $+\pi$ and chopper c2 shifts it by $-\pi$.

When we pulse the choppers on and off at a frequency f_c, an atom may receive a net phase shift of $\pm\pi$ or 0 depending on its velocity and the time at which it passed through the first chopper. Holmgren *et al.* [21] gives an intuitive explanation of how we measure contrast C vs f_c to determine v_0 and v_r. Fig. 3 shows an example of C vs f_c data. Hromada *et al.* [22] later improved upon Holmgren *et al.*'s model of C vs f_c by considering how the thickness and divergence of the beam causes some components of the atoms' velocity distribution to not be detected. In this work, we expanded our analysis to include the four interferometers shown in Fig. 1, performed a more in-depth error analysis, and added an additional calibration step to the measurement procedure.

Using phase choppers allows us to measure v_0 and v_r for Cs without needing to obtain resolved diffraction. In our earlier work, we measured v_0 and v_r by scanning the detector's x position to observe the atom diffraction pattern transmission through grating g1 [11]. However, since θ_d for Cs is so small, we would need a thinner detector wire and thinner collimating slits to resolve diffraction peaks, which would in turn reduce statistical precision.

Hromada *et al.* describes how the thickness and diver-

gence of the beam determines the likelihood for atoms of certain velocities to be detected [22]. The thickness and divergence is defined by the finite widths of the collimating slits w_1 and w_2. The finite width of the detector $w_{\rm det}$ and the detector's offset from the beamline in the x direction $\Delta x_{\rm det}$ also affect the probability of detecting atoms as a function of the atoms' velocities and initial positions in the apparatus. The phase and contrast we observe with our detector is that of an ensemble of atoms with different velocities, different incident positions on grating g1, and different incident angles on grating g1.

Uncertainties in w_1, w_2, $w_{\rm det}$, and $\Delta x_{\rm det}$ are more significant for beams that are physically wider. In K beams, which have larger θ_d of ≈ 50 μrad and wider velocity distributions ($\sigma_v = v_0/v_r \approx 2100/14$ m/s), more of the lower-velocity atoms in the distribution miss the detector. Therefore, uncertainties in the aforementioned quantities have a higher bearing on how we model the average velocity of *detected* atoms. Ignoring this component of the analysis would cause a systematic increase in measured v_0 by 0.5% and v_r by 10% for a typical K beam.

Modelling the four interferometers shown in Fig. 1, rather than only the $k = \pm 1$ interferometers, also improved our understanding of how likely it is for certain velocities to be detected. For K beams with wide velocity distributions, we would report v_0 too high by around 0.5% and v_r too low by around 5% if we only included the $k = \pm 1$ interferometers. This is because, for such beams, a much higher proportion of atoms in the $k = \pm 2$ interferometers miss the detector than in the $k = \pm 1$ interferometers. Ignoring the $k = \pm 2$ interferometers has a significant effect on the model of the detected $P(v)$ when the detected velocity distributions for the $k = \pm 1$ and $k = \pm 2$ interferometers are significantly different. Conversely, for Cs and Rb beams, we found no significant difference in results between models because most of the atoms in all interferometers were detected regardless of velocity.

Hromada *et al.* [22] also describes how inequality between L_1 and L_2 causes systematic errors. When $\Delta L = L_2 - L_1$ is nonzero, different paths through the interferometers have the best overlap at some z position within the beamline that is not exactly where grating g3 is located. Interference fringes acquire an additional phase in the laboratory frame of reference as components of each atom's wave function begin to separate. Stationary fringe phase is found (locally) along lines where the velocities of the components are equal but opposite. This effect magnifies or demagnifies the interference fringes that are formed at the third grating. We summarize this geometric magnification with the separation phase shift:

$$\Delta\Phi_{{\rm sep},k} = \frac{2\pi}{d_g}\left(\theta_{inc} + \frac{k}{2}\theta_d\right)\Delta L \qquad (6)$$

where k is the interferometer index (see Fig. 1) and $\theta_{\rm inc}$ is the incident angle on grating g1. To reduce systematic error in our v_0 and v_r measurements, we measure ΔL and set it equal to zero.

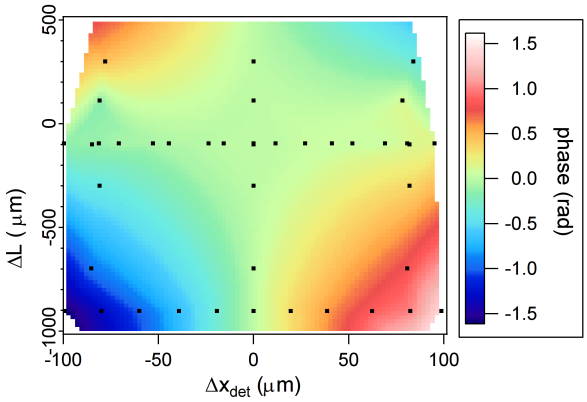

FIG. 4. (Color online) Data showing the phase of the interference fringes as a function of $\Delta x_{\rm det}$ and ΔL. The black dots represent coordinates at which data was acquired, and the colors represent contours inferred from the data. This figure shows how Φ vs $\Delta x_{\rm det}$ is a line with slope proportional to ΔL.

Eqn. (6) implies that uncertainty in ΔL is more significant for beams with larger θ_d, such as K beams. Also, because $\Delta\Phi_{{\rm sep},k}$ has a component proportional to $\theta_{\rm inc}$, uncertainty in ΔL is more significant for more divergent beams. As $|\Delta L|$ increases, uncertainties in w_1, w_2, $w_{\rm det}$, and $\Delta x_{\rm det}$ become more significant. Accordingly, we developed a method to set $\Delta L = 0$ to reduce those uncertainty contributions. Eqn. (6) implies that interferometers on either side of the beamline receive opposite phase shifts. Therefore, by moving the detector in the $\pm x$ direction, we observe linear changes in Φ as a function of $\Delta x_{\rm det}$ with slope ${\rm d}\Phi/{\rm d}x_{\rm det}$ proportional to ΔL. Fig. 4 shows data that demonstrates this effect. We set ΔL to 0 ± 30 μm by finding the ΔL for which ${\rm d}\Phi/{\rm d}x_{\rm det} = 0$.

Since we recalibrate ΔL every day, the 30 μm uncertainty in ΔL represents a systematic error for one day's measurements and a statistical error for many days' measurements averaged together. That error will contribute toward the statistical uncertainty of α measurements. The same is true for $\Delta x_{\rm det} = 0 \pm 30$ μm, which also fluctuates from day to day as we set up the apparatus.

If the interferometer grating bars are significantly nonvertical, it becomes necessary to consider the phase shift induced by the component of gravitational acceleration in the plane of the interferometer. That phase shift is given by

$$\Delta\Phi_{\rm accel} = \frac{\pi g \sin(\theta_g)(L_1 + L_2)^2}{2 d_g v^2} \qquad (7)$$

where θ_g is the tilt of the grating bars with respect to vertical [26]. Our interferometer's $|\theta_g|$ never exceeded 2.3 mrad. If we were to neglect this portion of the analysis,

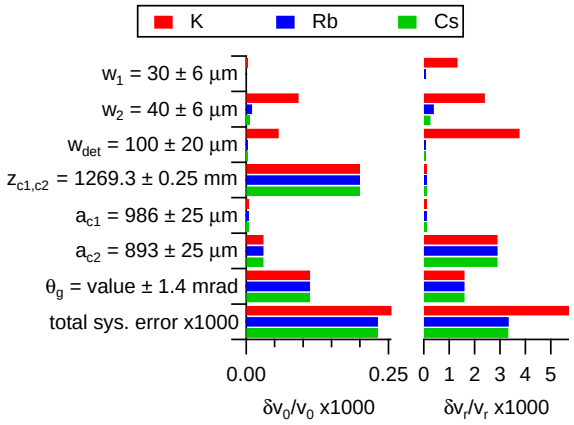

FIG. 5. (Color online) Systematic uncertainty budget for measurements of v_0 and v_r for our Cs, Rb, and K beams. The total systematic error in v_0 and v_r in turn contributes toward the total systematic uncertainty in α measurements (shown in Fig. 8). A nominal value for θ_g is not listed because θ_g changed from -2.37 ± 1.39 mrad to 1.73 ± 0.59 mrad toward the end of the experiment.

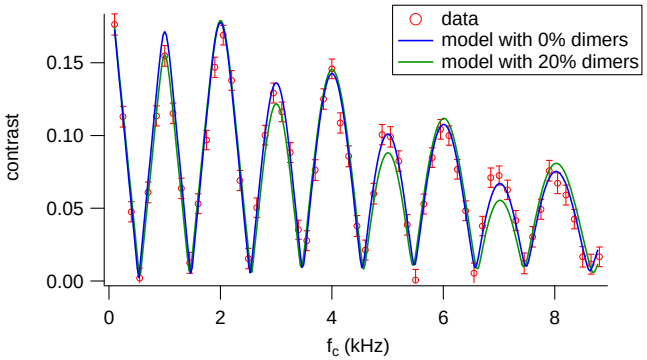

FIG. 6. (Color online) This figure illustrates how changing the fraction of dimers in the beam, f_d, affects the model of C vs f_c. The data (red) was first fit with a model (blue) in which the dimer fraction r_d was a fit parameter. The model best fit the data when $r_d = 0$. The model in green shows what C vs f_c would look like if v_0 and v_r were the same but r_d were equal to 0.2.

we would report v_0 incorrectly by up to 0.015% and v_r incorrectly by up to 0.25%.

The uncertainty budget for v_0 and v_r measurements is displayed in Fig. 5. The total statistical uncertainty in measured v_0 and v_r is roughly 10 times larger than the total systematic uncertainty after about 15 minutes of data acquisition with the phase choppers. Because v_0 and v_r drift over time, we measure the velocity distribution about every hour.

Atoms in an alkali metal gas have a small probability of forming homonuclear dimers, which have different polarizabilities than monomers. We were able to use the phase choppers data along with Molof *et al.*'s dimer-to-monomer polarizability ratios [27] to put an upper bound on the fraction of dimers in the beam. We inserted the dimer fraction r_d as an additional fit parameter to C vs f_c. The covariances among r_d, v_0, and v_r are all low, meaning that r_d is a sufficiently orthogonal fit paramter. Changing r_d affects the model of C vs f_c in a way that is different from how changing v_0 or v_r affects the model (see Fig. 6). Using this method, we determined that $r_d = 0$ with an uncertainty of 2%. We added this possibility of beams with 2% dimers to the error analysis of polarizability data, discussed in the next section.

II.c. Polarizability measurement

To measure the Cs, Rb, and K polarizability, we use two parallel, oppositely charged, 1/2-inch-diameter, stainless-steel pillars. The pillars are mounted to a single, rigid support structure so that a 3999.7 ± 1.0 μm gap exists between them. A motor moves the support structure in the $\pm x$ direction, and a length gauge monitors the structure's x position. The length gauge measures displacements of the structure with 30 nm accuracy. We begin a polarizability measurement with the assembly positioned such that the beam passes through the gap between the pillars near one of the edges. We take 25 sec of data with the electric field on and 25 sec with it off, and then move the pillars about 400 μm so that the beam approaches the other edge of the gap. We repeat this 9 times to observe the phase shift $\Delta\Phi = \Phi_{\text{pillars,on}} - \Phi_{\text{ref}}$ applied by the pillars as a function x_b (see an example in Fig. 7). We then repeat this sequence moving the pillars in the opposite direction in order to minimize possible systematic errors associated with travelling in a certain direction. When the electric field is off, we observe the reference phase Φ_{ref} and reference contrast C_{ref} given by

$$C_{\text{ref}} e^{i\Phi_{\text{ref}}} = C_0 e^{i\Phi_0} \frac{1}{2} \sum_{j=-1,1} \int_{v=0}^{\infty} P(v) e^{i\Delta\Phi_{\text{sag}}(v)} dv \quad (8)$$

The Sagnac phase, $\Delta\Phi_{\text{sag}}$, is a phase shift caused by the Earth's rotation and is described in [11, 28, 29]. C_0 is the contrast that would be observed in the absence of $\Delta\Phi_{\text{sag}}(v)$, and Φ_0 is an arbitrary phase constant. When the field is on, we instead observe

$$C_{\text{pillars,on}} e^{i\Phi_{\text{pillars,on}}} = C_0 e^{i\Phi_0} \frac{1}{2} \sum_{j=-1,1} \int_{v=0}^{\infty} P(v) e^{i\Delta\Phi_{\vec{E},j}(v,x_b) + i\Delta\Phi_{\text{sag}}(v)} dv \quad (9)$$

We fit a model to $\Delta\Phi$ vs x_b, as shown in Fig. 7. The fit parameters of that model are the polarizability and the pillars position x_{b0} for which the phase shift is null (i.e. the location of the virtual ground plane).

In our earlier work, we used one pillar next to a grounded plate instead of two pillars forming a virtual ground plane [11]. We measured x_b by eclipsing the beam

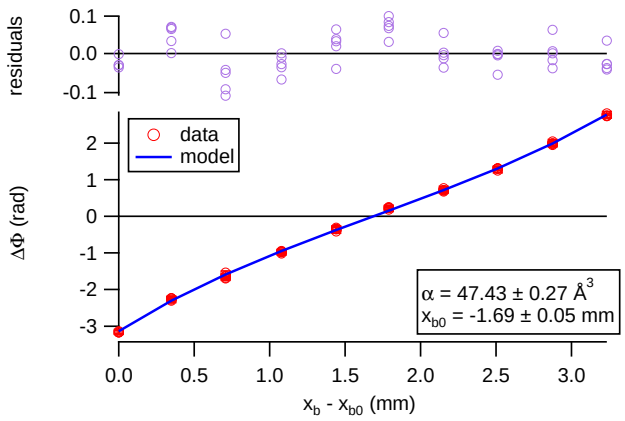

FIG. 7. (Color online) An example of a measurement of phase shift vs x position of the pillars for a Rb beam. The two fit parameters used to fit the model to these data are polarizability $\alpha_{\rm Rb}$ and the pillars' position at which the phase shift is null x_{b0}.

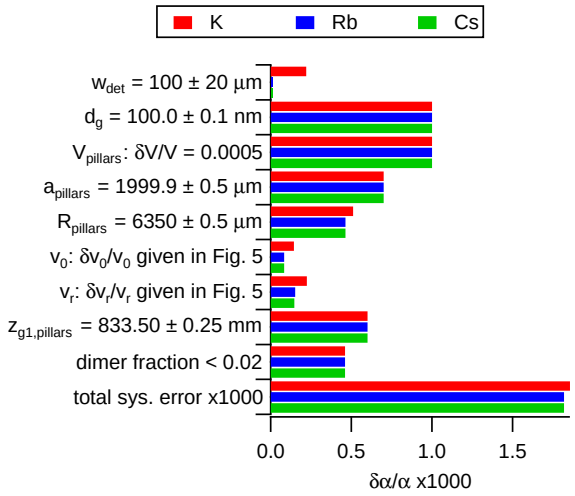

FIG. 8. (Color online) Systematic uncertainty budget for polarizability measurements for our Cs, Rb, and K beams. The uncertainties in knowledge of v_0 and v_r are propagated forward from Fig. 5. Values of $V_{\rm pillars}$ ranged from 5 kV to 7 kV, always with 0.05% uncertainty.

with the pillar. There were significant statistical errors of a few μm associated with this procedure, and a 1 μm error would lead to a 0.1% error in polarizability. Our new pillars assembly greatly reduces those statistical errors. Measuring $\Delta\Phi$ vs x_b on both sides of the ground plane makes our typical 50 μm uncertainties in x_{b0} add an insignificant amount of statistical uncertainty to the determined α.

The systematic uncertainty budget for our polarizability measurements is shown in Fig. 8. We constructed the new pillars using steel rods, the widths of which were accurately known to 1 μm.

We reduced the uncertainty in $V_{\rm pillars}$ to 0.05% by independently calibrating our voltage supplies. To measure $V_{\rm pillars}$, which ranged from 5 kV to 7 kV, we used a Fluke 80K-40 high voltage probe. We measured the probe's voltage divider constant, which itself depended on input voltage, using two Fluke 287 digital multimeters.

We measured $z_{g1,\rm pillars}$ to 1/4 mm accuracy. We placed rulers in the apparatus, after which three of us co-authors would read the rulers both live and from photographs. We repeated this process for many longitudinal positions of the rulers to further reduce statistical error in the measurement. Finally, we compared the rulers we used with other rulers to verify that the rulers we used were printed without significant systematic error. The value of $z_{g1,\rm pillars}$ we use in this analysis is the average of all those measurements.

We measured $a_{\rm pillars}$ to 0.5 μm accuracy by repeatedly scanning the pillars assembly across the beam and recording the positions at which each pillar half-eclipsed the beam. We repeated this procedure many times throughout the months during which we acquired our data to verify that $a_{\rm pillars}$ did not change over time.

For K beams with wide velocity distributions, we would report polarizability about 2% lower if we didn't take into account either the $k = \pm 2$ interferometers or the beam width and divergence.

Our θ_g was always close enough to zero such that we did not need to consider $\Delta\Phi_{\rm accel}$ in our polarizability data analysis. We would only need to consider $\Delta\Phi_{\rm accel}$ if $|\theta_g|$ exceeded 23 mrad. We also find that uncertainties in w_1 and w_2 each do not correspond to more than 0.004% uncertainty in α.

II.d. Determining the velocity distribution during polarizability measurements

A typical sequence of measurements is shown in Table II. We measure the velocity distribution twice between every four scans of the pillars across the beam, and calibrate the phase choppers between each pair of velocity measurements.

We linearly interpolate between v_0 and v_r measurements before and after each pillars scan to obtain those quantities at the time of that scan. Using cubic spline interpolation and Gaussian Process Regression to interpolate between v_0 and v_r measurements changes our reported polarizabilities by no more than 0.001%, which is small compared to our other uncertainties.

III. RESULTS AND DISCUSSION

Table III shows our measurements of Cs, Rb, and K polarizability and their statistical and systematic uncertainties. The statistical uncertainty reported is the standard error of the mean.

TABLE II. A typical sequence of measurements during a day of data acquisition. The $+x$ direction is arbitrarily chosen—the important aspect is that we spend an equal amount of time scanning the pillars in each direction so as to minimize possible systematic errors. This sequence of eight measurements is repeated once per hour for anywhere between 8 and 36 hours. We end the data acquisition by repeating the first four measurements.

Type of data acquired	Duration
contrast vs chopping freq.	7m 5s
chopper c1 phase	3m 45s
chopper c2 phase	3m 45s
contrast vs chopping freq.	7m 5s
$\Delta\Phi$ vs pillars position ($+x$ direction)	8m 45s
$\Delta\Phi$ vs pillars position ($-x$ direction)	8m 45s
$\Delta\Phi$ vs pillars position ($+x$ direction)	8m 45s
$\Delta\Phi$ vs pillars position ($-x$ direction)	8m 45s

TABLE III. Direct measurements of Cs, Rb, and K static, ground-state polarizabilities.

Atom	α(stat.)(sys.) (Å^3)
Cs	59.45(3)(11)
Rb	47.44(3)(9)
K	42.97(2)(8)

Table IV shows our measured ratios. Because we used the same apparatus for each direct measurement, most of the sources of systematic error summarized in Figs. 5 and 8 affect individual measurements in the same ways. These correlated uncertainties do not contribute toward systematic error of the ratios. Uncertainties in w_1, w_2, w_{det}, and ΔL contribute differently to systematic uncertainty in α_{Cs}, α_{Rb}, and α_{K} and therefore do also contribute toward the systematic uncertainties of the ratios. However, in our ratios, statistical uncertainties are almost 20 times higher than systematic uncertainties.

The fact that uncertainties in our polarizability ratios are dominated by statistical uncertainty suggests that we could use an atomic species with well-known polarizability, such as Li or metastable He, to calibrate our apparatus. We could use many weeks of Li and Cs polarizability measurements to report α_{Cs} with 0.01% uncertainty.

TABLE IV. Measured ratios of Cs, Rb, and K static, ground-state polarizabilities. The systematic errors in each ratio, which arise from the fact that the systematic errors in different measurements are not perfectly correlated, are negligible compared to the statistical errors.

Ratio	Value(stat.)	Sys. Err.
$\alpha_{\mathrm{Cs}}/\alpha_{\mathrm{K}}$	1.3835(9)	$5 \cdot 10^{-5}$
$\alpha_{\mathrm{Cs}}/\alpha_{\mathrm{Rb}}$	1.2532(10)	$6 \cdot 10^{-7}$
$\alpha_{\mathrm{Rb}}/\alpha_{\mathrm{K}}$	1.1040(9)	$4 \cdot 10^{-5}$

III.a. Comparisons with other experimental and theoretical polarizabilities

Fig. 9 compares our polarizability measurements with theoretical calculations, semi-empirical calculations, and experimental measurements subsequent to and including Molof *et al.*'s and Hall *et al.*'s 1974 measurements [4, 7]. Our α_{Rb} and α_{K} measurements improve upon previous direct measurements with results that have 2-5 times smaller uncertainty than [11] and 10 times smaller uncertainty than [7]. Our α_{Cs} measurement is consistent with Amini and Gould's [8] and has similar uncertainty. Amini and Gould's α_{Cs} measurement, in addition to being a 15× improvement in precision since the previous measurement by Molof *et al.* [7], is the only polarizability measurement using the fountain method. The consistency between our measurement and theirs serves as a cross-check for both methods.

Fig. 9 also compares our measured polarizability ratios to other theoretical, semi-empirical, and experimental ratios. Comparing polarizability ratios serves as a cross-check that is complementary to comparing direct measurements and calculated values. Since the fractional uncertainties on our measured ratios are smaller than those of our direct measurements, our ratios can be a more powerful test for theoretical calculations that predict α values consistent with our measurements. For example, Lim *et al.*'s 2005 α_{K} and α_{Rb} calculations agree to within 1.7 standard deviations of our measurements [45]. However, Lim *et al.*'s $\alpha_{\mathrm{Rb}}/\alpha_{\mathrm{K}}$ ratio is different from ours by over 7 standard deviations. As another example, the α_{K} predictions by Yong-Bo *et al.* in 2014 [53] and Lim *et al.* in 2005 [45] both agree well with α_{K} measurement, but those authors' α_{Cs} predictions are different from ours by around 7 standard deviations. Therefore, the $\alpha_{\mathrm{Cs}}/\alpha_{\mathrm{K}}$ ratios inferred from those authors' works differ from ours by 17 and 25 standard deviations, respectively.

III.b. Comparisons with polarizabilities derived from other quantities

Static polarizabilities can be related to electric dipole transition matrix elements, state lifetimes, oscillator strengths, and van der Waals coefficients. We will describe those relations and compare our α measurements to α values derived from recent calculations and high-precision measurements of those quantities; those comparisons are shown in Fig. 10.

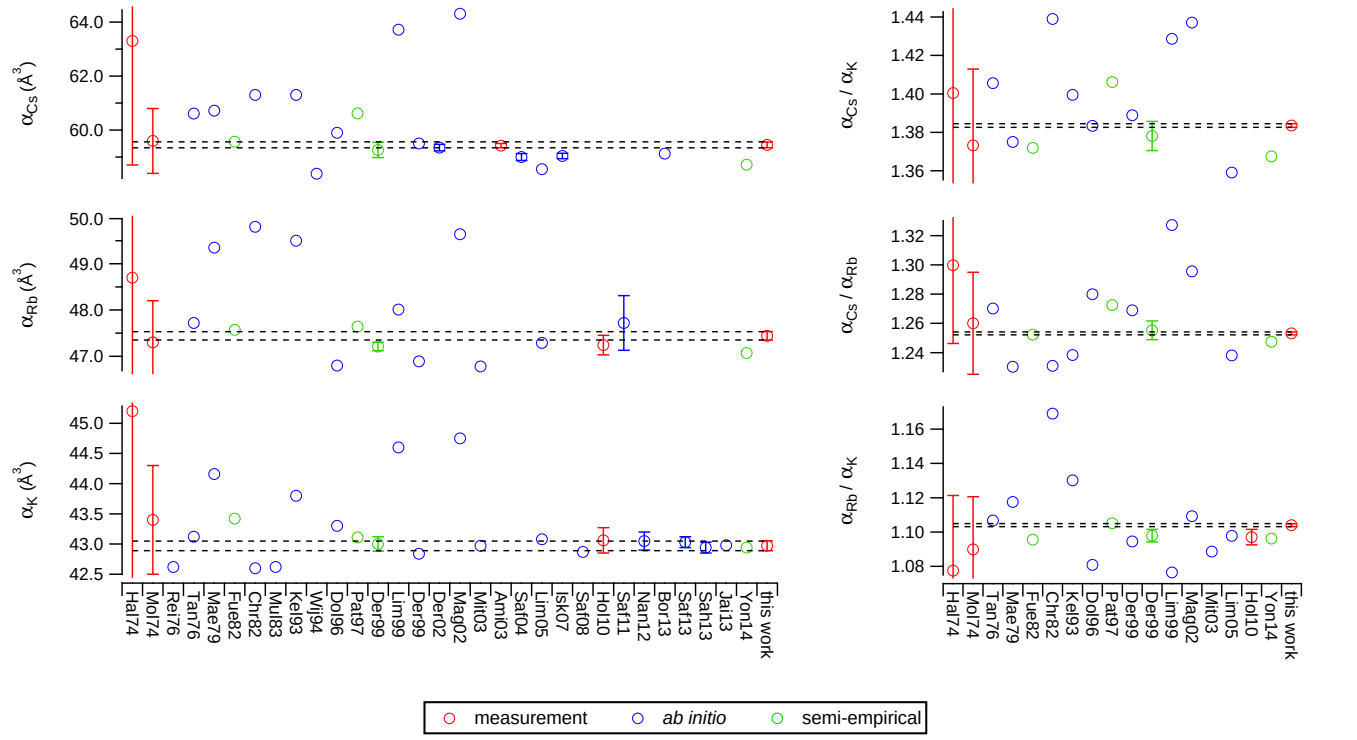

FIG. 9. (Color online) Our direct measurements (left) and measured ratios (right) compared with other measurements, *ab initio* calculations, and semi-empirical calculations [4, 7, 8, 11, 30–53]. The references are represented on the x-axis by the first three letters of the first author's last name followed by the year of publication. For the semi-empirical calculations: Reference Fue82 used semi-empirical pseudopotentials [34], Pat97 used experimentally-determined energy levels [39], Der99 used experimentally-determined electric dipole transition matrix elements [40], and Yon14 used semi-empirical core polarization potentials [53]. The error bars on the Mol74 ratios may overestimate the uncertainty because the authors did not discuss to what extent the correlated systematic uncertainties contributed to the uncertainties in the direct measurements.

TABLE V. We use the following residual polarizabilities α_r. The sources for α_r values are cited next to the values in the table.

Atom	α_r (Å^3)	
Cs	2.481(16)	[42]
Rb	1.562(89)	[67]
K	0.925(45)	[67]

The polarizability (in volume units) of an atom in state i can be written in terms of state lifetimes as

$$\alpha_i = \frac{c^3}{2}\sum_{k\neq i}\frac{1}{\tau_{ki}\omega_{ik}^4}\frac{g_k}{g_i} + \alpha_r \qquad (10)$$

where τ_{ki} is the lifetime associated with spontaneous decay from state k to i. ω_{ik} is the transition frequency between states i and k, and $g_n = 2J_n + 1$ is the degeneracy factor for state n. In our case, state i is the ground state. The residual polarizability α_r is the terms not explicitly included in the sum, the polarizability of the core electrons, and a correction accounting for correlations between core and valence electrons. We will explicitly sum over the principal transitions from $ns_{1/2}$ to $np_{1/2}$ and $np_{3/2}$, where $n = 6$ for Cs, $n = 5$ for Rb, and $n = 4$ for K, and we will include the other transitions in α_r. We abbreviate the lifetimes associated with the principal transitions to $\tau_{1/2}$ and $\tau_{3/2}$. In our calculations, we use the transition wavelengths ω_{0k} from references [68–71] and the α_r values indicated in Table V. Fig. 10 shows polarizabilities calculated using measurements of $\tau_{1/2}$ and $\tau_{3/2}$ [54–60]. Fig. 10 also shows $\alpha_{\rm Cs}$ calculated from values of $\tau_{1/2,\rm Rb}$ and $\tau_{3/2,\rm Rb}$ inferred in 2002 by Gutterres *et al.* from photo-association data taken in 2000 by Gabbanini *et al.* [62, 63].

We can use Patterson *et al.*'s 2015 measurement of $\tau_{3/2,\rm Cs}$ [72] along with a measurement of the ratio of principal transition matrix elements to report $\alpha_{\rm Cs}$. Rafac and Tanner measured the ratio of Cs electric dipole transition

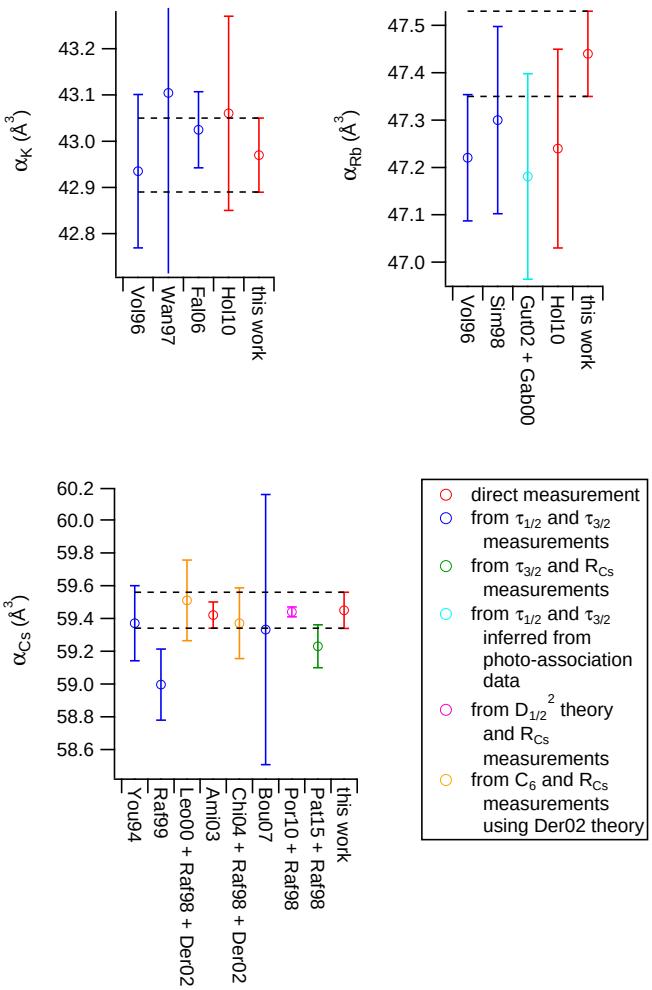

FIG. 10. (Color online) Comparisons of our lab's polarizability measurements and Amini and Gould's α_{Cs} measurement [8] to polarizabilities derived from measured lifetimes and lifetime ratios, [54–61], lifetimes inferred from photo-association data [62, 63], theoretical D^2 values [64], and van der Waals C_6 measurements [42, 65, 66].

matrix elements [61]

$$R_{\rm Cs} = \frac{\left|\left\langle 6s_{1/2}\right|\left|\hat{D}\right|\left|6p_{3/2}\right\rangle\right|^2}{\left|\left\langle 6s_{1/2}\right|\left|\hat{D}\right|\left|6p_{1/2}\right\rangle\right|^2} \tag{11}$$

which is related to the ratio of lifetimes

$$\frac{\tau_{1/2}}{\tau_{3/2}} = \frac{R_{\rm Cs}}{2}\left(\frac{\omega_{3/2}}{\omega_{1/2}}\right)^3 \tag{12}$$

We can also report a polarizability using $R_{\rm Cs}$ [61] in conjunction with Porsev *et al.*'s 2010 calculation of $D^2_{1/2,\rm Cs} = 20.334$ (in atomic units) [64]. We can write α_i in terms of the electric dipole transition matrix elements

TABLE VI. Matrix element ratios $R = D^2_{3/2}/D^2_{1/2}$ for Cs, Rb, and K. The sources for the ratios are cited next to the values in the table.

Atom	R	
Cs	1.9809(9)	[61]
Rb	1.99219(3)	[73]
K	1.9975(13)	[74]

as

$$\alpha_i = \frac{e^2}{12\pi\epsilon_0 a_0^4}\sum_{k\neq i}\frac{\left|\left\langle i\right|\left|\hat{D}\right|\left|k\right\rangle\right|^2}{\hbar\omega_{ik}} + \alpha_r \tag{13}$$

where a_0 is the Bohr radius. As before, we only explicitly consider the $ns_{1/2} - np_{1/2}$ and $ns_{1/2} - np_{3/2}$ matrix elements, where $ns_{1/2}$ is the ground state. We abbreviate the matrix elements associated with the principal transitions to $D_{1/2}$ and $D_{3/2}$.

In 2002, Derevianko and Porsev demonstrated a method for obtaining values of $D^2_{1/2,\rm Cs}$ and $D^2_{3/2,\rm Cs}$ from Cs van der Waals C_6 coefficients [42] and $R_{\rm Cs}$ [61]. Fig. 10 includes α values derived using experimental Cs C_6 measurements in conjunction with that method [65, 66].

III.c. Other atomic properties derived from our polarizability measurements

Finally, we use our polarizability measurements to report matrix elements, lifetimes, oscillator strengths, line strengths, and van der Waals C_6 coefficients. In these calculations, we use residual polarizabilities α_r from Table V and matrix element ratios R from Table VI. To report matrix elements and lifetimes, we use Eqn. (13) and Eqn. (11). α_i is given in terms of oscillator strengths f_{ik} as

$$\alpha_i = \frac{e^2}{4\pi\epsilon_0 m}\sum_{k\neq i}\frac{f_{ik}}{w^2_{ik}} + \alpha_r \tag{14}$$

where m is the electron mass. α_i is also given in terms of line strengths as

$$\alpha_i = \frac{1}{6\pi\epsilon_0\hbar}\sum_{k\neq i}\frac{S_{ki}}{g_i\omega_{ik}} + \alpha_r \tag{15}$$

C_6 can be expressed in terms of dynamic polarizability as

$$C_6 = \frac{3}{\pi}\int_0^\infty \alpha(i\omega)^2 d\omega \tag{16}$$

Derevianko *et al.*'s 2010 work tabulates values of $\alpha(i\omega)$

TABLE VII. Matrix elements, lifetimes, oscillator strengths, line strengths, and van der Waals C_6 coefficients calculated from our polarizability measurements. We used R values from Table VI. The matrix elements, line strengths, and C_6 coefficient are expressed in atomic units, while the lifetimes are expressed in SI units. δ_α, δ_R, and δ_{α_r} represent the uncertainties in the values due to uncertainty in α, R, and α_r, respectively. $\delta_{\rm tot}$ is the total uncertainty in the value. (-) represents a nonzero uncertainty of less than 0.5.

Quantity	Atom	Value	δ_α	δ_R	δ_{α_r}	$\delta_{\rm tot}$
$D_{1/2}$	Cs	4.510	(4)	(1)	(1)	(4)
	Rb	4.244	(4)	(-)	(4)	(6)
	K	4.105	(4)	(1)	(2)	(5)
$D_{3/2}$	Cs	6.348	(6)	(-)	(1)	(6)
	Rb	5.990	(6)	(-)	(6)	(8)
	K	5.802	(6)	(1)	(3)	(6)
$\tau_{1/2}$ (ns)	Cs	34.74	(7)	(1)	(1)	(7)
	Rb	27.53	(5)	(-)	(5)	(8)
	K	26.76	(5)	(1)	(3)	(6)
$\tau_{3/2}$ (ns)	Cs	30.33	(6)	(-)	(1)	(6)
	Rb	26.13	(5)	(-)	(5)	(7)
	K	26.43	(5)	(1)	(3)	(6)
$f_{1/2}$	Cs	0.345	(1)	(-)	(-)	(1)
	Rb	0.344	(1)	(-)	(1)	(1)
	K	0.332	(1)	(-)	(-)	(1)
$f_{3/2}$	Cs	0.718	(1)	(-)	(-)	(1)
	Rb	0.699	(1)	(-)	(1)	(2)
	K	0.667	(1)	(-)	(1)	(1)
$S_{1/2}$	Cs	20.34	(4)	(1)	(1)	(4)
	Rb	18.01	(4)	(-)	(3)	(5)
	K	16.85	(3)	(1)	(2)	(4)
$S_{3/2}$	Cs	40.30	(8)	(1)	(1)	(8)
	Rb	35.89	(7)	(-)	(7)	(10)
	K	33.66	(6)	(1)	(4)	(7)
C_6	Cs	6892	(24)	(-)	(0)	(24)
	Rb	4734	(17)	(-)	(0)	(17)
	K	3891	(15)	(-)	(0)	(15)

for Cs, Rb, and K atoms among others [75]. To derive C_6 values from our $\alpha(0)$ measurements, we modify Derevianko *et al.*'s values of $\alpha(i\omega)$ and $\alpha(0)$ thus:

$$\alpha_{\rm new}(i\omega) = \alpha(i\omega) - [\alpha_{\text{this work}}(0) - \alpha(0)]\,\frac{\alpha_p(i\omega)}{\alpha_p(0)} \quad (17)$$

In the above equation, $\alpha_p(i\omega)$ is the contribution to $\alpha(i\omega)$ by the principle transitions. The ratio $\alpha_p(i\omega)/\alpha_p(0)$ is given by

$$\frac{\alpha_p(i\omega)}{\alpha_p(0)} = \frac{\frac{1}{\omega_{1/2}^2+\omega^2} + \frac{R\frac{\omega_{1/2}}{\omega_{3/2}}}{\omega_{3/2}^2+\omega^2}}{\frac{1}{\omega_{1/2}^2} + \frac{R\omega_{1/2}}{\omega_{3/2}}} \quad (18)$$

TABLE VIII. Excited state polarizabilities $\alpha_{np_{1/2}}$, where $n = 6$ for Cs, $n = 5$ for Rb, and $n = 4$ for K. The values were calculated using our measurements and $\alpha_{np_{1/2}} - \alpha_{ns_{1/2}}$ measurements [76, 77].

Atom	$\alpha_{np_{1/2}}$
Cs	196.87(11)
Rb	120.38(9)
K	89.96(8)

Predictions of the parity-non-conserving coupling strength, $E_{\rm PNC}$, in Cs depends heavily on $D_{1/2}$. We note that our Cs $D_{1/2}$ value is consistent with the theoretical Cs $D_{1/2}$ calculated by Porsev *et al.* in 2010 for the purpose of interpreting PNC data [64].

Finally, we use our measurements together with recent measurements of Cs, Rb, and K $\alpha_{np_{1/2}} - \alpha_{ns_{1/2}}$ [76, 77] to report excited state polarizabilities $\alpha_{np_{1/2}}$ with better than 0.09% uncertainty. These results are shown in Table VIII and serve as benchmark tests for calculations of dipole transition matrix elements for $p - d$ transitions.

IV. OUTLOOK

We are currently exploring ways to measure the polarizability of either Li or metastable He, the polarizabilities of which can be easily calculated. By measuring $\alpha_{\rm Cs}/\alpha_{\rm He*}$ or $\alpha_{\rm Cs}/\alpha_{\rm Li}$, we could report a direct measurement of $\alpha_{\rm Cs}$ with precision comparable to that of the ratios reported here for the benefit of PNC research. Such a measurement would also act as a calibration of the measurements presented in this work, because it would be independent of systematic errors that may affect our direct measurements.

We are also exploring electron-impact ionization schemes for atom detection, which would allow us to detect most atoms and molecules. Our Langmuir-Taylor detector only allows us to detect alkali metals and some alkaline-Earth metals [18]. Installing an electron-impact ionization detector would allow us to broaden the scope of atom interferometry as a precision measurement tool.

This work is supported by NSF Grant No. 1306308 and a NIST PMG. M.D.G. and R.T. are grateful for NSF GRFP Grant No. DGE-1143953 for support.

[1] J. Mitroy, M. S. Safronova, and C. W. Clark, J. Phys. B **44**, 202001 (2010).
[2] H. Scheffers and J. Stark, Phys. Z. **35**, 625 (1934).
[3] G. E. Chamberlain and J. C. Zorn, Phys. Rev. **129**, 677 (1963).
[4] W. D. Hall and J. C. Zorn, Phys. Rev. A **10**, 1141 (1974).

[5] L. Ma, J. Indergaard, B. Zhang, I. Larkin, R. Moro, and W. A. de Heer, Phys. Rev. A **91**, 010501 (2015).
[6] A. Salop, E. Pollack, and B. Bederson, Phys. Rev. **124**, 1431 (1961).
[7] R. W. Molof, H. L. Schwartz, T. M. Miller, and B. Bederson, Phys. Rev. A **10**, 1131 (1974).
[8] J. M. Amini and H. Gould, Phys. Rev. Lett. **91**, 153001 (2003).
[9] C. R. Ekstrom, J. Schmiedmayer, M. S. Chapman, T. D. Hammond, and D. E. Pritchard, Phys. Rev. A **51**, 3883 (1995).
[10] A. Miffre, M. Jacquey, M. Büchner, G. Trénec, and J. Vigué, Eur. Phys. J. D **38**, 353 (2006).
[11] W. F. Holmgren, M. C. Revelle, V. P. Lonij, and A. D. Cronin, Phys. Rev. A **81**, 053607 (2010).
[12] M. Berninger, A. Stefanov, S. Deachapunya, and M. Arndt, Phys. Rev. A **76**, 013607 (2007).
[13] P. Berman, ed., *Atom Interferometry* (Academic Press, San Diego, 1997).
[14] A. D. Cronin, J. Schmiedmayer, and D. E. Pritchard, Rev. Mod. Phys. **81**, 1051 (2009).
[15] D. Cho, C. S. Wood, S. C. Bennett, J. L. Roberts, and C. E. Wieman, Phys. Rev. A **55**, 1007 (1997).
[16] M.-A. Bouchiat and C. Bouchiat, Reports Prog. Phys. **60**, 1351 (1997).
[17] V. A. Dzuba, J. C. Berengut, V. V. Flambaum, and B. Roberts, Phys. Rev. Lett. **109**, 203003 (2012).
[18] R. Delhuille, A. Miffre, E. Lavallette, M. Büchner, C. Rizzo, G. Trénec, J. Vigué, H. J. Loesch, and J. P. Gauyacq, Rev. Sci. Instrum. **73**, 2249 (2002).
[19] T. D. Roberts, *Measuring Atomic Properties with an Atom Interferometer*, Ph.D. thesis, M.I.T. (2002).
[20] T. D. Roberts, A. D. Cronin, M. V. Tiberg, and D. E. Pritchard, Phys. Rev. Lett. **92**, 060405 (2004).
[21] W. F. Holmgren, I. Hromada, C. E. Klauss, and A. D. Cronin, New J. Phys. **13**, 115007 (2011).
[22] I. Hromada, R. Trubko, W. F. Holmgren, M. D. Gregoire, and A. D. Cronin, Phys. Rev. A **89**, 033612 (2014).
[23] G. Scoles, D. Bassi, U. Buck, and D. Lainé, eds., *Atomic and Molecular Beam Methods* (Oxford University Press, New York, Oxford, 1988).
[24] C. R. Ekstrom, *Experiments with a Separated Beam Atom Interferometer*, Ph.D. thesis, M.I.T. (1993).
[25] D. A. Kokorowski, *Measuring Decoherence and the Matter-wave Index of Refraction with an Improved Atom Interferometer by*, Ph.D. thesis, M.I.T. (2001).
[26] J. Greenberg, *An atom interferometer gyroscope*, Undergraduate honors thesis, U. of Arizona (2014).
[27] R. W. Molof, T. M. Miller, H. L. Schwartz, B. Bederson, and J. T. Park, J. Chem. Phys. **61**, 1816 (1974).
[28] A. Lenef, T. Hammond, E. Smith, M. Chapman, R. Rubenstein, and D. Pritchard, Phys. Rev. Lett. **78**, 760 (1997).
[29] M. Jacquey, A. Miffre, G. Trénec, M. Büchner, J. Vigué, and A. Cronin, Phys. Rev. A **78**, 013638 (2008).
[30] K. T. Tang, J. Chem. Phys. **64**, 3063 (1976).
[31] E. A. Reinsch and W. Meyer, Phys. Rev. A **14**, 915 (1976).
[32] W. Kutzelnigg and F. Maeder, Chem. Phys. **35**, 397 (1979).
[33] P. A. Christiansen and K. S. Pitzer, Chem. Phys. Lett. **85**, 434 (1982).
[34] P. Fuentealba, J. Phys. B **15**, L555 (1982).
[35] W. Müller, J. Flesch, and W. Meyer, J. Chem. Phys. **80**, 3297 (1984).
[36] V. Kello and A. J. Sadlej, Phys. Rev. A **47**, 1715 (1993).
[37] W. A. van Wijngaarden and J. Li, J. Quant. Spectrosc. Radiat. Transf. **52**, 555 (1994).
[38] M. Dolg, Theor. Chim. Acta **93**, 141 (1996).
[39] S. H. Patil and K. T. Tang, J. Chem. Phys. **106**, 2298 (1997).
[40] A. Derevianko, W. R. Johnson, M. S. Safronova, and J. F. Babb, Phys. Rev. Lett. **82**, 3589 (1999).
[41] S. Magnier and M. Aubert-Frécon, J. Quant. Spectrosc. Radiat. Transf. **75**, 121 (2002).
[42] A. Derevianko, Phys. Rev. A **65**, 053403 (2002).
[43] J. Mitroy and M. Bromley, Phys. Rev. A **68**, 052714 (2003).
[44] M. S. Safronova and C. W. Clark, Phys. Rev. A **69**, 040501 (2004).
[45] I. S. Lim, P. Schwerdtfeger, B. Metz, and H. Stoll, J. Chem. Phys. **122**, 104103 (2005).
[46] U. I. Safronova and M. S. Safronova, Phys. Rev. A **78**, 052504 (2008).
[47] M. S. Safronova and U. I. Safronova, Phys. Rev. A **83**, 052508 (2011).
[48] D. K. Nandy, Y. Singh, B. P. Shah, and B. K. Sahoo, Phys. Rev. A **86**, 052517 (2012).
[49] J. Jiang, L. Y. Tang, and J. Mitroy, Phys. Rev. A **87**, 032518 (2013).
[50] B. K. Sahoo and B. Arora, Phys. Rev. A **87**, 023402 (2013).
[51] M. S. Safronova, U. I. Safronova, and C. W. Clark, Phys. Rev. A **87**, 052504 (2013).
[52] a. Borschevsky, V. Pershina, E. Eliav, and U. Kaldor, Phys. Rev. A **87**, 022502 (2013).
[53] T. Yong-Bo, L. Cheng-Bin, and Q. Hao-Xue, Chin. Phys. B **23**, 063101 (2014).
[54] L. Young, W. T. Hill, S. J. Sibener, S. D. Price, C. E. Tanner, C. E. Wieman, and S. R. Leone, Phys. Rev. A **50**, 2174 (1994).
[55] R. Rafac, C. Tanner, A. Livingston, and H. Berry, Phys. Rev. A **60**, 3648 (1999).
[56] N. Bouloufa, A. Crubellier, and O. Dulieu, Phys. Rev. A **75**, 052501 (2007).
[57] S. Falke, I. Sherstov, E. Tiemann, and C. Lisdat, J. Chem. Phys. **125**, 224303 (2006).
[58] U. Volz and H. Schmoranzer, Phys. Scr. **T65**, 48 (1996).
[59] J. Simsarian, L. Orozco, G. Sprouse, and W. Zhao, Phys. Rev. A **57** (1998).
[60] H. Wang, J. Li, X. T. Wang, C. J. Williams, P. L. Gould, and W. C. Stwalley, Phys. Rev. A **55**, R1569 (1997).
[61] R. Rafac and C. Tanner, Phys. Rev. A **58**, 1087 (1998).
[62] C. Gabbanini, A. Fioretti, A. Lucchesini, S. Gozzini, and M. Mazzoni, Phys. Rev. Lett. **84**, 2814 (2000).
[63] R. Gutterres, C. Amiot, A. Fioretti, C. Gabbanini, M. Mazzoni, and O. Dulieu, Phys. Rev. A **66**, 024502 (2002).
[64] S. G. Porsev, K. Beloy, and A. Derevianko, Phys. Rev. D **82**, 036008 (2010).
[65] P. Leo, C. Williams, and P. Julienne, Phys. Rev. Lett. **85**, 2721 (2000).
[66] C. Chin, V. Vuletić, A. J. Kerman, S. Chu, E. Tiesinga, P. J. Leo, and C. J. Williams, Phys. Rev. A **70**, 032701 (2004).
[67] M. S. Safronova, B. Arora, and C. W. Clark, Phys. Rev. A **73**, 022505 (2006).
[68] V. Gerginov, C. E. Tanner, S. a. Diddams, A. Bartels,

and L. Hollberg, Opt. Lett. **30**, 1734 (2005).
[69] V. Gerginov, K. Calkins, C. E. Tanner, J. J. McFerran, S. Diddams, A. Bartels, and L. Hollberg, Phys. Rev. A **73**, 032504 (2006).
[70] S. Falke, E. Tiemann, C. Lisdat, H. Schnatz, and G. Grosche, Phys. Rev. A **74**, 032503 (2006).
[71] I. Johansson, Ark. foer Fys. **20**, 135 (1961).
[72] B. M. Patterson, J. F. Sell, T. Ehrenreich, M. A. Gearba, G. M. Brooke, J. Scoville, and R. J. Knize, Phys. Rev. A **91**, 012506 (2015).
[73] R. H. Leonard, a. J. Fallon, C. a. Sackett, and M. S. Safronova, (2015), arXiv:1507.07898.
[74] R. Trubko, Prep. (2015).
[75] A. Derevianko, S. G. Porsev, and J. F. Babb, At. Data Nucl. Data Tables **96**, 323 (2010).
[76] L. R. Hunter, D. Krause, D. J. Berkeland, and M. G. Boshier, Phys. Rev. A **44**, 6140 (1992).
[77] K. E. Miller, D. Krause, and L. R. Hunter, Phys. Rev. A **49**, 5128 (1994).